Emergence of monolayer electron behavior in bulk van der Waals superlattice

Pengfei Ding,[1,*] Jun-Fa Lin,[1,*] Peihan Sun,[2,*] Rui Lou,[3,4,5,*] Alexander Fedorov,[3,4,5] Zhi-Xiao He,[1,6] Huan Ma,[1,6] Zuoping Zhou,[7] Bernd Büchner,[3,9] Xi Chen,[7,8] Kai Liu,[1,6] Tian-Long Xia,[1,6,†] and Shancai Wang[1,6,‡]

[1]*Department of Physics, Key Laboratory of Quantum State Construction and Manipulation (Ministry of Education), Renmin University of China, Beijing 100872, China*
[2]*Department of Physics, School of Science, Hebei University of Science and Technology, Shijiazhuang, 050018 Hebei, China*
[3]*Leibniz Institute for Solid State and Materials Research, IFW Dresden, 01069 Dresden, Germany*
[4]*Helmholtz-Zentrum Berlin für Materialien und Energie, Albert-Einstein-Straße 15, 12489 Berlin, Germany*
[5]*Joint Laboratory "Functional Quantum Materials" at BESSY II, 12489 Berlin, Germany*
[6]*Beijing Key Laboratory of Optoelectronic Functional Materials & Micro-Nano Devices, Renmin University of China, Beijing 100872, China*
[7]*Department of Physics, Tsinghua University, Beijing 100084, China*
[8]*Frontier Science Center for Quantum Information, Beijing 100084, China*
[9]*Institute for Solid State and Materials Physics, TU Dresden, 01062 Dresden, Germany*

(Received 2 November 2023; revised 1 February 2024; accepted 26 February 2024; published 3 April 2024)

Monolayer transition metal dichalcogenides (TMDs) have a simple crystal structure, but they exhibit intricate physical phenomena that differ from their bulk counterparts. Recently, there has been significant interest in the electronic behavior of monolayer TMDs hosted in a natural van der Waals superlattice material, $Ba_6Nb_{11}S_{28}$, consisting of alternating NbS_2 monolayers and block layers. Here, we report the electronic structure study of $Ba_6Nb_{11}S_{28}$ and $Ba_6Ta_{11}S_{28}$. Using angle-resolved photoemission spectroscopy and density functional theory calculation, we show that the electronic structures of the superlattices are similar to those of monolayer TMDs. The two-dimensional characteristics indicate that the interlayer coupling of adjacent TMD layers is suppressed by the intercalation of the Ba_3NbS_5 or Ba_3TaS_5 block layer. A clear band splitting due to spin-orbital coupling is observed in $Ba_6Ta_{11}S_{28}$, while no obvious splitting is found in $Ba_6Nb_{11}S_{28}$. These observations are in qualitative agreement with the observation on monolayer films of NbS_2 and TaS_2. Based on our findings, these natural superlattices can serve as an effective model system for studying monolayer materials and their potential applications.

DOI: 10.1103/PhysRevB.109.155115

I. INTRODUCTION

Transition metal dichalcogenides (TMDs) consist of a stack of two-dimensional (2D) atomic layers and exhibit complex and diverse physical phenomena. Many of these physical phenomena, such as charge density waves (CDW), superconductivity, spin-valley locking, and Mott insulators, have attracted considerable attention [1–5]. As TMDs are reduced to the monolayer limit, these properties may intertwine, giving rise to puzzling phenomena such as direct band gaps, nontrivial topology, and Ising superconductivity [6–9]. Meanwhile, the evolution of bulk properties into the 2D limit has also been of great interest [10–17]. The CDW phase of monolayer NbS_2 and TaS_2 exhibits obvious substrate dependence [17–21]. Superconductivity is suppressed in monolayer NbS_2, but enhanced in TaS_2 [13–16,22,23].

Most 2D TMDs are produced through film growth or mechanical exfoliation of bulk crystals. However, both methods suffer from inherent instability in natural environments. For example, exposure to air causes rapid oxidation and the loss of superconductivity in monolayer NbS_2 [13]. In the case of film growth, the choice of substrate influences the physical properties of the resulting material. For instance, the use of an Au (111) substrate disrupts the CDW order in monolayer NbS_2 and TaS_2 [18,19]. Additionally, the electronic hybridization between the sample and its metallic substrate induces a "pseudodoping" effect, leading to a significant change in the band structure [24]. Thus, finding a new way to realize a clean 2D TMD material becomes a significant challenge.

Recently, a van der Waals superlattice $Ba_6Nb_{11}S_{28}$, consisting of alternating block layers and monolayer TMDs, has provided a different approach for fabricating 2D materials [25,26]. With the insertion of block layers, the interlayer coupling between the nearest-neighbor monolayer TMDs diminishes or even vanishes, permitting the monolayer TMD to exist inside the block layer. Transport measurements indicate that $Ba_6Nb_{11}S_{28}$ is a clean 2D superconductor with $T_c = 0.82$ K, and its Cooper pairs could form 2D bosonic Landau levels under magnetic field [25,27]. In this study, we measured the electronic structure of $Ba_6M_{11}S_{28}$ (M = Nb, Ta) using angle-resolved photoemission spectroscopy (ARPES) technique and made a comparison to the results of a

*Pengfei Ding, Jun-Fa Lin, Peihan Sun, and Rui Lou contributed equally to this work.
†tlxia@ruc.edu.cn
‡scw@ruc.edu.cn

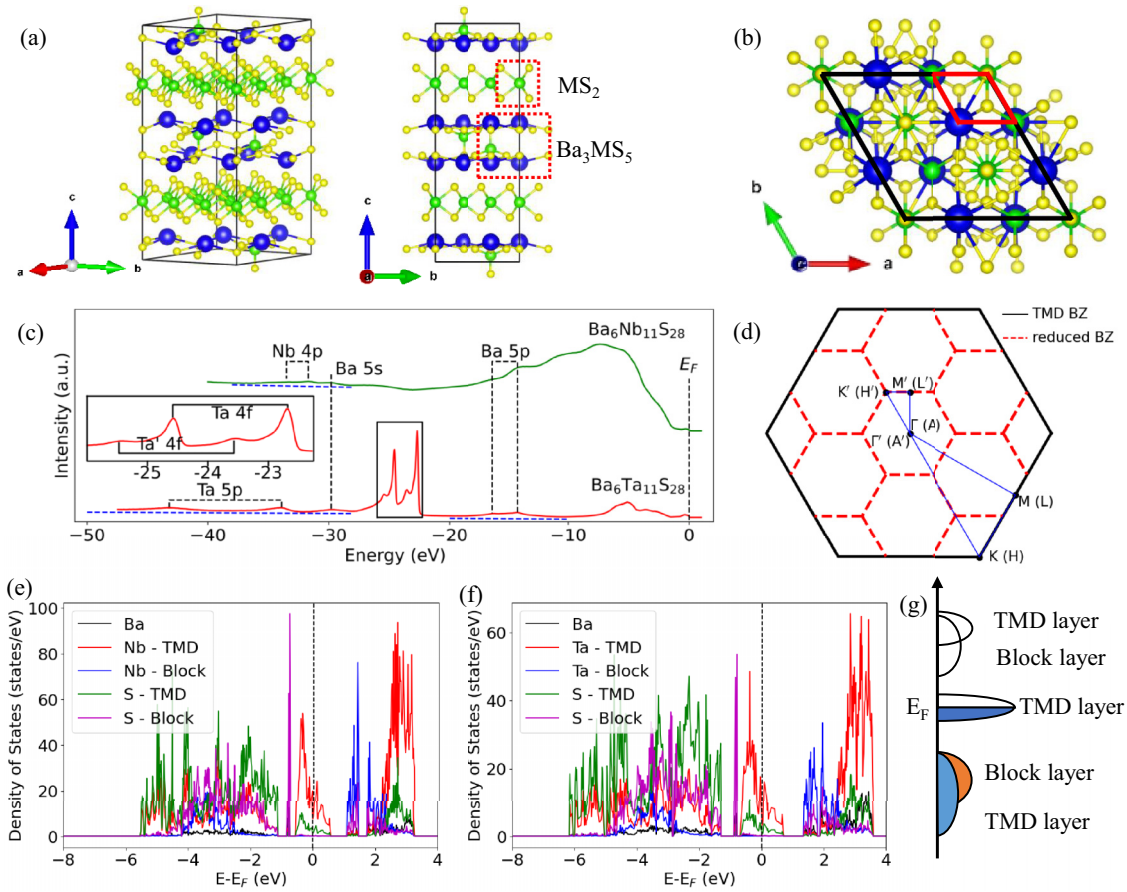

FIG. 1. Crystal structures and shallow core levels of $Ba_6Nb_{11}S_{28}$ and $Ba_6Ta_{11}S_{28}$. (a) Schematic representation of the crystal structures for the $Ba_6Nb_{11}S_{28}$ and $Ba_6Ta_{11}S_{28}$, where Ba_3MS_5 (M = Nb, Ta) layers are intercalated in the H-MS_2 lattice. (b) Top view of crystal structures. The large black rhombus represents the conventional cell of $Ba_6M_{11}S_{28}$. The small red rhombus corresponds to the conventional cell of MS_2. (c) Core-level spectra for $Ba_6Nb_{11}S_{28}$ and $Ba_6Ta_{11}S_{28}$, respectively. The linear background intensity is indicated by the blue dotted line. (d) Top view of two hexagonal BZs. The black hexagon corresponds to the BZ of MS_2. The red dotted lines represent reduced BZ formed by a 3×3 superlattice. (e),(f) DFT calculated layer- and element-resolved DOSs of $Ba_6Nb_{11}S_{28}$ and $Ba_6Ta_{11}S_{28}$, respectively. (g) Schematic plot of electronic DOSs of $Ba_6M_{11}S_{28}$.

density-functional-theory (DFT) calculation. The chemical formula of $Ba_6M_{11}S_{28}$ can be interpreted as $(Ba_3MS_5)_2(MS_2)_9$, where the crystal structure consists of an alternatively stacked monolayer MS_2 and Ba_3MS_5 layer along the c axis [Fig. 1(a)]. Our research indicates that in comparison with bulk 2H-MS_2, the interlayer coupling is effectively suppressed, consequently transforming the electronic structure of $Ba_6M_{11}S_{28}$ into the 2D limit. Our findings demonstrate that the $Ba_6M_{11}S_{28}$ family provides a different platform for hosting and manipulating TMDs in a 2D limit.

II. METHOD

Single crystals were synthesized using a molten salt flux method [25]. Crystal structures and lattice constants are determined using transmission electron microscopes. ARPES measurements were conducted at the BL07U and BL09U endstations of the Shanghai Synchrotron Radiation Facility with a Scienta DA30-L electron analyzer and the 1^2-ARPES endstation of the UE-112-PGM2 beam line at the Helmholtz-Zentrum Berlin BESSY-II light source. The angular and energy resolutions were set to better than 0.1° and 5 meV, respectively. During the experiments, the sample temperature was maintained at $T = 20$ K unless specified otherwise, and the vacuum conditions were kept better than 6×10^{-11} Torr.

The DFT calculations were performed by using the projector augmented-wave method [28,29] as implemented in the Vienna *ab initio* simulation package (VASP) [30,31]. The generalized gradient approximation (GGA) in the scheme of Perdew-Burke-Ernzerhof [32] was adopted for the exchange-correlation functional. The energy cutoff of the plane-wave basis was set to 380 eV. The Fermi surface was broadened by the Gaussian smearing method with a width of 0.05 eV. A $5 \times 5 \times 3$ Monkhorst-Pack k-point mesh was adopted to sample the 3D Brillouin zone (BZ). Both lattice constants and internal atomic positions were optimized. The convergence tolerances of force and energy were set to 0.01 eV/Å and 10^{-5} eV, respectively. The DFT-D2 method [33,34] was used to account for the interlayer van der Waals interaction. For convenient comparison, the band structures of 3×3 supercells were unfolded to unit cells by using the band unfolding method [35] as in the PYVASPWFC package [36]. For convenience, we use Γ-M-K-A-H-L-A ($\bar{\Gamma}$-$\bar{M}$-$\bar{K}$) for the TMD

(surface) BZ, noted as TMD BZ, and Γ'-M'-K'-A'-H'-L' for the BZ of $Ba_6M_{11}S_{28}$, also noted as reduced BZ.

III. RESULTS

Figures 1(a) and 1(b) show the crystal structures of $Ba_6M_{11}S_{28}$ (M=Nb, Ta). The lattice constants of $Ba_6Nb_{11}S_{28}$ ($Ba_6Ta_{11}S_{28}$) are $a = b = 9.66$ (9.62) Å and $c = 24.13$ (24.14) Å. Both of them exhibit the same hexagonal structure with the space group $P\bar{3}1c$. The superlattice can be viewed as the alternate stacking of monolayer 1H-MS_2 and block layer Ba_3MS_5 along the c axis. In the top view [Fig. 1(b)], each layer comprises 3×3 MS_2. In the shallow core-level photoemission spectroscopy [Fig. 1(c)], the Ba 5s and 5p peaks are clearly observed at $E_F - 29.8$, $E_F - 14.2$, and $E_F - 16.3$ eV, respectively, for both $Ba_6Ta_{11}S_{28}$ and $Ba_6Nb_{11}S_{28}$. For $Ba_6Ta_{11}S_{28}$, two sharp Ta 4f peaks are located at $E_F - 22.7$ and $E_F - 24.6$ eV, respectively. Furthermore, two satellite peaks are present on the left side of the Ta 4f core levels [inner plot of Fig. 1(c)]. These peaks are from the Ta atoms of the Ba_3TaS_5 and TaS_2 layers, respectively.

The DFT-calculated projected density of states (DOS) are shown in Figs. 1(e) and 1(f), for $Ba_6Nb_{11}S_{28}$ and $Ba_6Ta_{11}S_{28}$, respectively. In addition, a schematic drawing of the band structure is shown in Fig. 1(g). It is evident that the electron states near the Fermi level (E_F) predominantly originate from NbS_2 and TaS_2 (highlighted by the green and red curves). Conversely, states away from the E_F arise from the Ba_3NbS_5 and Ba_3TaS_5 layers (mixed with deep states from the TMD layer), positioned approximately 1 eV above and below the E_F. Energy gaps are observed between the contributions from the TMD layer and the block layer, one located at above E_F and another one below E_F. Consequently, the electronic structure near the E_F of $Ba_6M_{11}S_{28}$ could be understood as nearly isolated monolayer 1H-MS_2 separated by insulating Ba_3MS_5 layers.

The band structures of $Ba_6M_{11}S_{28}$ (where M = Nb and Ta), calculated using DFT without spin-orbital coupling (SOC), are presented in Fig. 2. No dispersive band with respect to k_z is observed near the E_F. This is qualitatively in contrast to the behavior observed in 2H-MS_2 (M = Ta, Nb), where a rapidly dispersive band originating from the S p_z orbital exists in the vicinity of E_F [37–40]. Given the presence of a 3×3 superstructure in the MS_2 layer within the unit cell, a zone folding effect is expected. We calculated the unfolded band structure with respect to the MS_2 unit cell, and present it in Figs. 2(b) and 2(d). The unfolded band structure aligns more closely with the band structure from the monolayer calculation [15,16,18,19,37], showing a negligible contribution from the folding effect, indicated by the light-blue shadows in Figs. 2(b) and 2(d).

The measured band structures of $Ba_6M_{11}S_{28}$ (M = Nb, Ta) are depicted in Fig. 3. For $Ba_6Nb_{11}S_{28}$, two isotropic holelike Fermi pockets centered at 2D BZ high-symmetry points $\bar{\Gamma}$ and $\bar{K}$ are identified [Figs. 3(a) and 3(b)]. In comparison, the band structure of $Ba_6Ta_{11}S_{28}$ exhibits distinct features [Figs. 3(d) and 3(e)]. Instead of only one band existing near the E_F for $Ba_6Nb_{11}S_{28}$, two bands are visually evident for $Ba_6Ta_{11}S_{28}$, as indicated by the dashed lines in Figs. 3(b) and 3(e). As a result, the Fermi surface around $\bar{K}$ clearly splits into two circles, and the Fermi surfaces around $\bar{\Gamma}$ show hexagonal-like shapes instead of circular ones. These observed features are

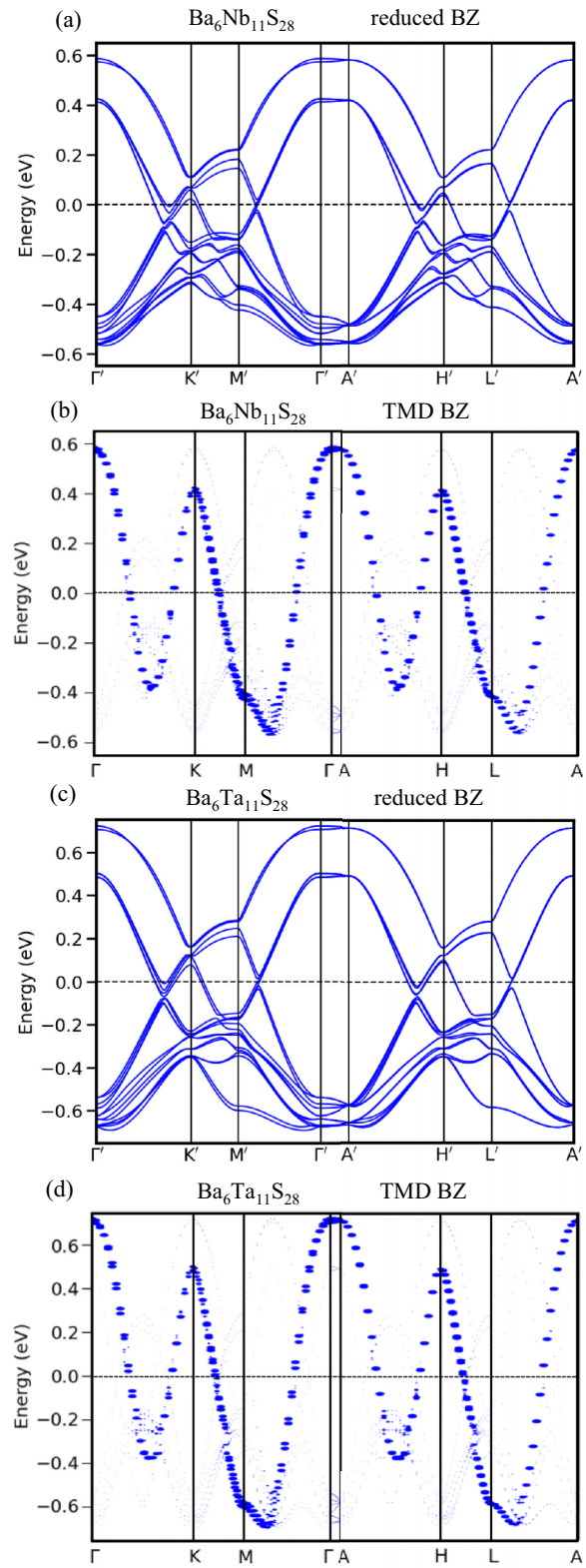

FIG. 2. DFT calculated band structures of $Ba_6Nb_{11}S_{28}$ and $Ba_6Ta_{11}S_{28}$ without SOC. (a) Band structure of $Ba_6Nb_{11}S_{28}$. (b) Band structure of $Ba_6Nb_{11}S_{28}$ unfolded into the NbS_2 BZ. (c),(d) The same as (a),(b), but for $Ba_6Ta_{11}S_{28}$.

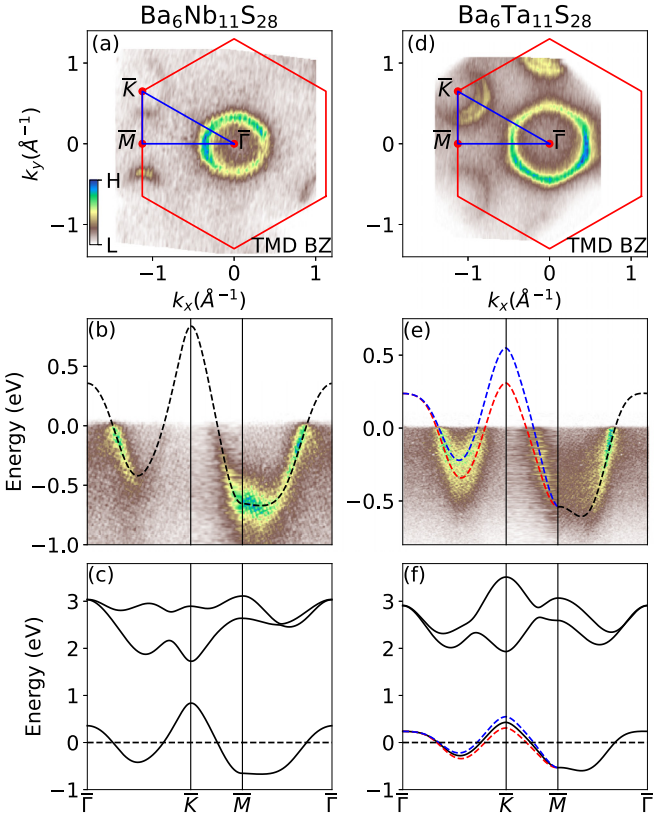

FIG. 3. In-plane band structures of $Ba_6Nb_{11}S_{28}$ and $Ba_6Ta_{11}S_{28}$. (a) ARPES intensity plots at E_F for $Ba_6Nb_{11}S_{28}$. The plot has been integrated with a ± 15 meV centered at E_F. The red line represents the TMD BZ, and the color scale shown is used in all other image plots. (b) Band structure of $Ba_6Nb_{11}S_{28}$ along the high-symmetry momentum paths $\overline{\Gamma}$–$\overline{K}$–$\overline{M}$–$\overline{\Gamma}$, as indicated by the blue line in (a). The tight-binding calculated band structure is overlaid with a black dotted line. (c) Tight-binding calculated band structure of monolayer NbS_2 without SOC. (d)–(f) Equivalent to (a)–(c), but for $Ba_6Ta_{11}S_{28}$. The band splitting due to SOC is depicted as blue and red dotted lines in (f).

qualitatively in agreement with the results of monolayer NbS_2 and TaS_2. [18,19].

Based on previous DFT calculations, when the TMD material is reduced to the monolayer limit, the bandwidth of the S p_z states decreases, and the band position shifts away from the E_F [10,37,41]. Consequently, for $Ba_6Nb_{11}S_{28}$, the Fermi surfaces originate entirely from one electron band, which exhibits out-of-plane Nb d_{z^2} character around $\overline{\Gamma}$ and in-plane Nb d_{xy/x^2-y^2} character around $\overline{K}$. To account for the electron behavior similar to monolayers, a three-band third-nearest-neighbor tight-binding model with the Nb/Ta orbital basis of (d_{z^2}, d_{xy}, $d_{x^2-y^2}$) was utilized [41]. The fitted dispersion is shown in Fig. 3(c), and the corresponding parameters are listed in Table I. For $Ba_6Ta_{11}S_{28}$, SOC needs to be introduced into the tight-binding model to describe the splitting of the band [Fig. 3(f)]. The reconstructed tight-binding band structures agree quantitatively well with our measurements in band dispersion and Fermi surface topology, suggesting that the block layers have less impact on the band structure of the TMD layer.

TABLE I. Tight-binding parameters (in eV) obtained through fitting the measured band structure. The specific algorithms and notations follow Ref. [41]. Initial numerical values for the fit were sourced from Refs. [46,47]. ϵ_1 and ϵ_2 denote the on-site energy for d_{z^2} and $d_{x^2-y^2}/d_{xy}$ orbitals, respectively. t, r, u are nearest-neighbor, next-nearest-neighbor, and third-nearest-neighbor hopping parameters, respectively. λ denotes the SOC strength.

Parameter	Notation	$Ba_6Nb_{11}S_{28}$	$Ba_6Ta_{11}S_{28}$
On site	ϵ_1	0.9775	1.4466
	ϵ_2	2.5438	1.8496
Nearest neighbor	t_0	−0.087	−0.256
	t_1	0.4	0.2568
	t_2	0.3339	0.405
	t_{11}	0.1057	0.277
	t_{12}	0.12	0.2787
	t_{12}	0.005	−0.087
Next-nearest neighbor	r_0	0.1124	0.0037
	r_1	−0.02	−0.0997
	r_2	0.11	0.0385
	r_{11}	0.0191	0.032
	r_{12}	−0.0069	0.0986
Third-nearest neighbor	u_0	−0.0649	0.0685
	u_1	0.0276	−0.0381
	u_2	−0.0301	0.0535
	u_{11}	0.1572	0.0601
	u_{12}	−0.078	−0.0179
	u_{22}	−0.0082	−0.0425
Spin-orbital coupling	λ	0	0.12

The insertion of the Ba_3MS_5 block layer reduces the interlayer coupling and makes the band structure more two dimensional. Figure 4 presents the photon-energy ($h\nu$) dependence of the band structure for both $Ba_6M_{11}S_{28}$ (M = Nb, Ta). From the intensity map at the E_F in the $h\nu$–$k_\parallel$ plane, the Fermi momenta show no variation over a wide range of photon energies, spanning several Brillouin zones along k_z [Figs. 4(a) and 4(c)]. Figures 4(b) and 4(d) show the energy-momentum (E–k) intensity maps at several typical photon energies. The band dispersion near the E_F remains the same and is in good agreement with the tight-binding calculations. Notably, along the $\overline{\Gamma}$–$\overline{K}$ direction, the band splitting is not discernible in $Ba_6Nb_{11}S_{28}$ [Fig. 4(b)] and the band clearly splits into two branches in $Ba_6Ta_{11}S_{28}$ [Fig. 4(d)]. In $Ba_6Ta_{11}S_{28}$, the two branches still show no k_z dependence with variations in photon energy [Figs. 4(e) and 4(f)]. All these features indicate the 2D electron behavior in $Ba_6Nb_{11}S_{28}$ and $Ba_6Ta_{11}S_{28}$.

We estimated the charge carrier density in $Ba_6Nb_{11}S_{28}$ and $Ba_6Ta_{11}S_{28}$ by calculating their Fermi surface volumes. By measuring the areas of the two holelike Fermi surfaces located at $\overline{\Gamma}$ and $\overline{K}$ in $Ba_6Nb_{11}S_{28}$, as well as the corresponding spin-split Fermi surfaces in $Ba_6Ta_{11}S_{28}$, we extracted the carrier intensities of these systems. The volume ratios of the hole Fermi surfaces to the Brillouin zone are approximately 22.5% for $Ba_6Nb_{11}S_{28}$ and around 29.1% for $Ba_6Ta_{11}S_{28}$. This corresponds to approximately 1.55 electrons per NbS_2 and 1.42 electrons per TaS_2, respectively. In comparison to bulk MS_2, each MS_2 accepts approximately 0.55 (about 5/9) electron for NbS_2 and around 0.42 (about 4/9) electron for TaS_2.

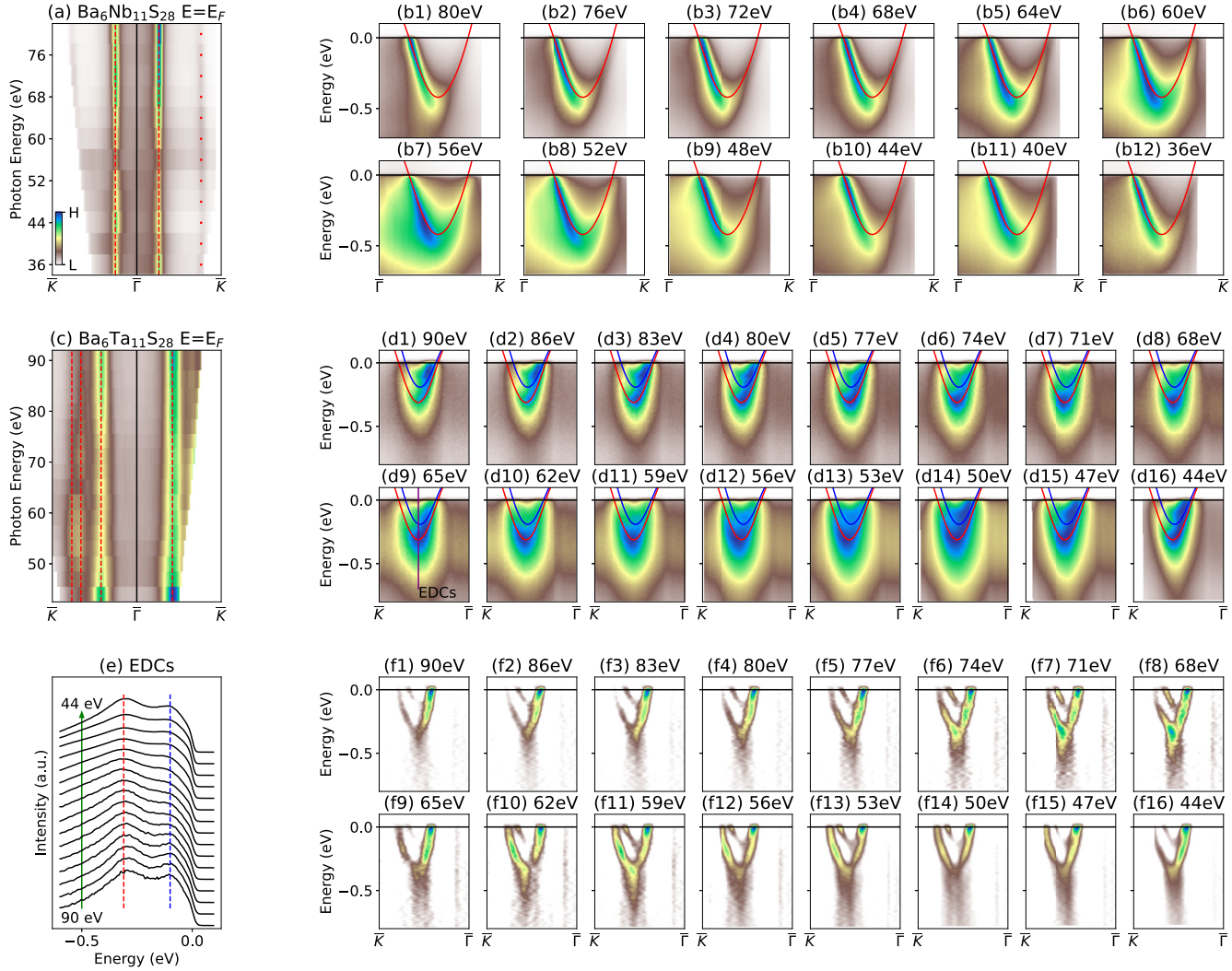

FIG. 4. Out-of-plane band structures of $Ba_6Nb_{11}S_{28}$ and $Ba_6Ta_{11}S_{28}$. (a) Photon-energy-dependent ARPES intensity of $Ba_6Nb_{11}S_{28}$ at E_F along the $\overline{\Gamma}$-$\overline{K}$ direction. Plot has been integrated with ± 15 meV centered at E_F, and the color scale shown is used in all other image plots. (b) Band structure plots of $Ba_6Nb_{11}S_{28}$ along $\overline{\Gamma}$-$\overline{K}$ collected at various photon energies. (c),(d) Equivalent to (a),(b), but for $Ba_6Ta_{11}S_{28}$. The purple line in (d9) indicates the momentum location of the energy distribution curves (EDCs) shown in (e). (e) Stacks of EDCs taken at the point of maximum band splitting. (f) Corresponding second-derivative plots of (d).

In a unit cell of $Ba_6M_{11}S_{28}$, there exist nine MS_2 and two Ba_3MS_5. Thus, the block layer Ba_3MS_5 transfers 5 electrons to the NbS_2 layer and 4 electrons to the TaS_2 layer, respectively.

IV. DISCUSSION

It is common that bulk TMD materials with a 2H structure exhibit superconductivity and CDW [1]. With a double-layer structure and interlayer coupling, bulk 2H-MX_2 (M = Nb, Ta, and X = S, Se) displays double-walled Fermi surface contours around the $\overline{\Gamma}$ and $\overline{K}$ points [4,39,42,43]. In the monolayer limit (with a 1H structure), only a single band with no obvious band splitting was observed in monolayer NbS_2/Au(111) [18]. ARPES experiments have shown that the monolayer TaS_2/Au(111) exhibits a band splitting caused by SOC, leading to the breaking of spin degeneracy [19]. However, a side effect of a monolayer TMD on top of a metallic substrate Au(111) is the strong hybridization between the TMD and substrate. This hybridization creates a "pseudodoping" effect, where the substrate significantly influences the band structure of the monolayer, even without obvious charge transfer [24]. Here, the band structures of the intercalated $Ba_6M_{11}S_{28}$ (M = Nb, Ta) around the E_F are entirely attributed to the MS_2 layer, which is consistent with the monolayer results calculated by DFT [15,37,41]. In the vicinity of E_F, there is no electron state from the block layer. Furthermore, photon-energy-dependent measurements reveal that the band exhibits negligible variation along the k_z direction, indicating that $Ba_6M_{11}S_{28}$ possesses quasi-2D band structures.

Recent studies have shown that a 2D band structure could be achieved by a natural van der Waals superlattice [44,45]. By inserting ionic liquid or a block layer into bulk 2H-$NbSe_2$, the interlayer coupling of the TMD layer can be reduced. With intercalations, the p_z orbital of chalcogens shifts away from the E_F. The system transfers from a 2H structure with 3D characteristics to a 1H structure with more 2D-like features. In $Ba_6M_{11}S_{28}$, the TMD layer and the block layer are

coupled by weak van der Waals interactions. The interlayer interaction between TMD layers becomes negligible because of the insertion of the block layer and large separation along the c axis. Although the intercalated block layer has a larger unit cell or superstructure, its impact on the band structure of the TMD layer would be suppressed due to the weak coupling between the TMD and block layers. Furthermore, any disorder or sample defects in the block layer further reinforces this suppression, and make the zone folding effect less observable. Therefore, we propose that $Ba_6M_{11}S_{28}$ is an ideal candidate for hosting a 2D electron gas in a three-dimensional crystal.

In comparison with monolayers grown on metallic substrates, the crystal structure of a van der Waals superlattice could offer higher crystal quality and better stability. Bulk 2H-NbS_2 exhibits a superconductivity transition with T_c at around 6 K [21,48]. When it is artificially exfoliated to the monolayer, the superconductivity vanishes [13,14]. The suppression of superconductivity in monolayer NbS_2 is explained by the disorder resulting from the incorporation of atmospheric oxygen [13]. In $Ba_6Nb_{11}S_{28}$, the NbS_2 layers are protected by the block layers. A superconducting transition temperature of $T_c \sim 0.82$ K is observed [25]. This T_c value can be regarded as a reasonable extrapolation of T_c with a decrease in layer thickness. Meanwhile, the superconductivity transition temperature (zero resistance temperature) increases from $T_c \leqslant 1$ K for the bulk TaS_2 to about 2 K with the reduction of thickness [15,16,23,49,50]. In $Ba_6Ta_{11}S_{28}$, under the protection provided by the block layer, the transition temperature further increases to 2.6 K [51].

The absence of inversion symmetry in monolayer MX_2 results in a significant spin-orbit splitting of the states at the $\overline{K}$ valleys and their inversion partner $\overline{K}'$ [3,52]. Due to the combination of SOC and broken inversion symmetry, the spins near $\overline{K}$ and $\overline{K}'$ align to be antiparallel along the out-of-plane direction. This gives rise to a noteworthy phenomenon known as Ising superconductivity, whose superconducting phase survives in the presence of an in-plane magnetic field that considerably exceeds the Pauli limit [52]. Spin-valley locking has been observed in bulk 2H-$NbSe_2$ and the monolayer $NbSe_2$ has been identified as an Ising superconductor [4,9,53–55]. The large splitting of the band in $Ba_6Ta_{11}S_{28}$ and the small band splitting in $Ba_6Nb_{11}S_{28}$ suggest a stronger SOC with Ta than Nb, making $Ba_6Ta_{11}S_{28}$ an ideal candidate for spin-locking-related phenomena.

V. SUMMARY

In summary, we present an investigation of the electronic structure of the natural van der Waals superlattices $Ba_6Nb_{11}S_{28}$ and $Ba_6Ta_{11}S_{28}$. The band structure of these compounds exhibits significant similarities to that of monolayer TMDs. Photon-energy-dependent measurements show almost no dispersion in the out-of-plane direction. These findings suggest that the intercalated block layers can effectively disrupt the interlayer coupling between adjacent TMD layers. Clear band splitting is observed only in $Ba_6Ta_{11}S_{28}$, and it is not strong in $Ba_6Nb_{11}S_{28}$. This splitting is attributed to the stronger SOC of Ta compared to Nb. Consequently, our findings suggest that $Ba_6M_{11}S_{28}$ (M = Nb, Ta) can serve as a valuable tool for tailoring dimensionality and investigating low-dimensional physics.

The data that support the findings of this study are available from the corresponding author upon reasonable request.

ACKNOWLEDGMENTS

This work is supported by the National Key R & D Program of China (Grants No.2022YFA1403800, No. 2019YFA0308602, and No. 2022YFA1403103), and the National Natural Science Foundation of China (Grants No. 11774421, No. 12074425, and No. 11874422). The work at IFW and HZB was supported by the Deutsche Forschungsgemeinschaft under Grant No. SFB 1143 (Project No. C04) and the Würzburg-Dresden Cluster of Excellence on Complexity and Topology in Quantum Matter–ct.qmat (EXC 2147, Project ID No. 390858490). B.B. acknowledges the support from the BMBF via Project No. UKRATOP. Computational resources were provided by the Physical Laboratory of High-Performance Computing at Renmin University of China.

[1] S. Manzeli, D. Ovchinnikov, D. Pasquier, O. V. Yazyev, and A. Kis, Nat. Rev. Mater. **2**, 17033 (2017).
[2] C. Heil, S. Poncé, H. Lambert, M. Schlipf, E. R. Margine, and F. Giustino, Phys. Rev. Lett. **119**, 087003 (2017).
[3] D. Xiao, G.-B. Liu, W. Feng, X. Xu, and W. Yao, Phys. Rev. Lett. **108**, 196802 (2012).
[4] L. Bawden, S. P. Cooil, F. Mazzola, J. M. Riley, L. J. Collins-McIntyre, V. Sunko, K. W. B. Hunvik, M. Leandersson, C. M. Polley, T. Balasubramanian, T. K. Kim, M. Hoesch, J. W. Wells, G. Balakrishnan, M. S. Bahramy, and P. D. C. King, Nat. Commun. **7**, 11711 (2016).
[5] Y. D. Wang, W. L. Yao, Z. M. Xin, T. T. Han, Z. G. Wang, L. Chen, C. Cai, Y. Li, and Y. Zhang, Nat. Commun. **11**, 4215 (2020).
[6] K. F. Mak, C. Lee, J. Hone, J. Shan, and T. F. Heinz, Phys. Rev. Lett. **105**, 136805 (2010).
[7] Y.-T. Hsu, A. Vaezi, M. H. Fischer, and E.-A. Kim, Nat. Commun. **8**, 14985 (2017).
[8] J. M. Lu, O. Zheliuk, I. Leermakers, N. F. Q. Yuan, U. Zeitler, K. T. Law, and J. T. Ye, Science **350**, 1353 (2015).
[9] X. Xi, Z. Wang, W. Zhao, J.-H. Park, K. T. Law, H. Berger, L. Forró, J. Shan, and K. F. Mak, Nat. Phys. **12**, 139 (2016).
[10] A. Kuc, N. Zibouche, and T. Heine, Phys. Rev. B **83**, 245213 (2011).
[11] P. Wu, X. Peng, C. Luo, Z. Li, and J. Zhong, Phys. Rev. B **105**, 174105 (2022).
[12] D. Lin, S. Li, J. Wen, H. Berger, L. Forró, H. Zhou, S. Jia, T. Taniguchi, K. Watanabe, X. Xi, and M. S. Bahramy, Nat. Commun. **11**, 2406 (2020).
[13] R. Yan, G. Khalsa, B. T. Schaefer, A. Jarjour, S. Rouvimov, K. C. Nowack, H. G. Xing, and D. Jena, Appl. Phys. Express **12**, 023008 (2019).

[14] Z. Wang, C.-Y. Cheon, M. Tripathi, G. M. Marega, Y. Zhao, H. G. Ji, M. Macha, A. Radenovic, and A. Kis, ACS Nano **15**, 18403 (2021).
[15] S. C. de la Barrera, M. R. Sinko, D. P. Gopalan, N. Sivadas, K. L. Seyler, K. Watanabe, T. Taniguchi, A. W. Tsen, X. Xu, D. Xiao, and B. M. Hunt, Nat. Commun. **9**, 1427 (2018).
[16] Y. Yang, S. Fang, V. Fatemi, J. Ruhman, E. Navarro-Moratalla, K. Watanabe, T. Taniguchi, E. Kaxiras, and P. Jarillo-Herrero, Phys. Rev. B **98**, 035203 (2018).
[17] H. Lin, W. Huang, K. Zhao, C. Lian, W. Duan, X. Chen, and S.-H. Ji, Nano Res. **11**, 4722 (2018).
[18] R.-M. Stan, S. K. Mahatha, M. Bianchi, C. E. Sanders, D. Curcio, P. Hofmann, and J. A. Miwa, Phys. Rev. Mater. **3**, 044003 (2019).
[19] C. E. Sanders, M. Dendzik, A. S. Ngankeu, A. Eich, A. Bruix, M. Bianchi, J. A. Miwa, B. Hammer, A. A. Khajetoorians, and P. Hofmann, Phys. Rev. B **94**, 081404(R) (2016).
[20] J. Hall, N. Ehlen, J. Berges, E. van Loon, C. van Efferen, C. Murray, M. Rösner, J. Li, B. V. Senkovskiy, M. Hell, M. Rolf, T. Heider, M. C. Asensio, J. Avila, L. Plucinski, T. Wehling, A. Grüneis, and T. Michely, ACS Nano **13**, 10210 (2019).
[21] I. Guillamón, H. Suderow, S. Vieira, L. Cario, P. Diener, and P. Rodière, Phys. Rev. Lett. **101**, 166407 (2008).
[22] C.-S. Lian, C. Heil, X. Liu, C. Si, F. Giustino, and W. Duan, Phys. Rev. B **105**, L180505 (2022).
[23] E. Navarro-Moratalla, J. O. Island, S. Mañas-Valero, E. Pinilla-Cienfuegos, A. Castellanos-Gomez, J. Quereda, G. Rubio-Bollinger, L. Chirolli, J. A. Silva-Guillén, N. Agraït, G. A. Steele, F. Guinea, H. S. J. Van Der Zant, and E. Coronado, Nat. Commun. **7**, 11043 (2016).
[24] B. Shao, A. Eich, C. Sanders, A. S. Ngankeu, M. Bianchi, P. Hofmann, A. A. Khajetoorians, and T. O. Wehling, Nat. Commun. **10**, 180 (2019).
[25] A. Devarakonda, H. Inoue, S. Fang, C. Ozsoy-Keskinbora, T. Suzuki, M. Kriener, L. Fu, E. Kaxiras, D. C. Bell, and J. G. Checkelsky, Science **370**, 231 (2020).
[26] K. Ma, S. Jin, F. Meng, Q. Zhang, R. Sun, J. Deng, L. Chen, L. Gu, G. Li, and Z. Zhang, Phys. Rev. Mater. **6**, 044806 (2022).
[27] A. Devarakonda, T. Suzuki, S. Fang, J. Zhu, D. Graf, M. Kriener, L. Fu, E. Kaxiras, and J. G. Checkelsky, Nature (London) **599**, 51 (2021).
[28] P. E. Blöchl, Phys. Rev. B **50**, 17953 (1994).
[29] G. Kresse and D. Joubert, Phys. Rev. B **59**, 1758 (1999).
[30] G. Kresse and J. Hafner, Phys. Rev. B **47**, 558 (1993).
[31] G. Kresse and J. Furthmüller, Comput. Mater. Sci. **6**, 15 (1996).
[32] J. P. Perdew, K. Burke, and M. Ernzerhof, Phys. Rev. Lett. **77**, 3865 (1996).
[33] X. Wu, M. C. Vargas, S. Nayak, V. Lotrich, and G. Scoles, J. Chem. Phys. **115**, 8748 (2001).
[34] S. Grimme, J. Comput. Chem. **27**, 1787 (2006).
[35] V. Popescu and A. Zunger, Phys. Rev. B **85**, 085201 (2012).
[36] Q. Zheng, VASP band unfolding (2018), https://github.com/QijingZheng/VaspBandUnfolding.
[37] C. Heil, M. Schlipf, and F. Giustino, Phys. Rev. B **98**, 075120 (2018).
[38] D. Huang, H. Nakamura, K. Küster, U. Wedig, N. B. M. Schröter, V. N. Strocov, U. Starke, and H. Takagi, Phys. Rev. B **105**, 245145 (2022).
[39] Z. El Youbi, S. W. Jung, C. Richter, K. Hricovini, C. Cacho, and M. D. Watson, Phys. Rev. B **103**, 155105 (2021).
[40] R. Zhao, B. Grisafe, R. K. Ghosh, S. Holoviak, B. Wang, K. Wang, N. Briggs, A. Haque, S. Datta, and J. Robinson, 2D Mater. **5**, 025001 (2018).
[41] G.-B. Liu, W.-Y. Shan, Y. Yao, W. Yao, and D. Xiao, Phys. Rev. B **88**, 085433 (2013).
[42] J. Zhao, K. Wijayaratne, A. Butler, J. Yang, C. D. Malliakas, D. Y. Chung, D. Louca, M. G. Kanatzidis, J. van Wezel, and U. Chatterjee, Phys. Rev. B **96**, 125103 (2017).
[43] S. V. Borisenko, A. A. Kordyuk, A. N. Yaresko, V. B. Zabolotnyy, D. S. Inosov, R. Schuster, B. Büchner, R. Weber, R. Follath, L. Patthey, and H. Berger, Phys. Rev. Lett. **100**, 196402 (2008).
[44] H. Zhong, H. Zhang, H. Zhang, T. Bao, K. Zhang, S. Xu, L. Luo, A. Rousuli, W. Yao, J. D. Denlinger, Y. Huang, Y. Wu, Y. Xu, W. Duan, and S. Zhou, Phys. Rev. Mater. **7**, L041801 (2023).
[45] H. Zhang, A. Rousuli, K. Zhang, L. Luo, C. Guo, X. Cong, Z. Lin, C. Bao, H. Zhang, S. Xu, R. Feng, S. Shen, K. Zhao, W. Yao, Y. Wu, S. Ji, X. Chen, P. Tan, Q.-K. Xue, Y. Xu *et al.*, Nat. Phys. **18**, 1425 (2022).
[46] W.-Y. He, B. T. Zhou, J. J. He, N. F. Q. Yuan, T. Zhang, and K. T. Law, Commun. Phys. **1**, 40 (2018).
[47] T. Machida, Y. Kohsaka, K. Iwaya, R. Arita, T. Hanaguri, R. Suzuki, M. Ochi, and Y. Iwasa, Phys. Rev. B **96**, 075206 (2017).
[48] J. Kačmarčík, Z. Pribulová, C. Marcenat, T. Klein, P. Rodière, L. Cario, and P. Samuely, Phys. Rev. B **82**, 014518 (2010).
[49] J. M. E. Harper, T. H. Geballe, and F. J. DiSalvo, Phys. Rev. B **15**, 2943 (1977).
[50] S. Nagata, T. Aochi, T. Abe, S. Ebisu, T. Hagino, Y. Seki, and K. Tsutsumi, J. Phys. Chem. Solids **53**, 1259 (1992).
[51] J.-F. Lin and T.-L. Xia (private communication).
[52] D. Wickramaratne, S. Khmelevskyi, D. F. Agterberg, and I. I. Mazin, Phys. Rev. X **10**, 041003 (2020).
[53] Y. Xing, K. Zhao, P. Shan, F. Zheng, Y. Zhang, H. Fu, Y. Liu, M. Tian, C. Xi, H. Liu, J. Feng, X. Lin, S. Ji, X. Chen, Q.-K. Xue, and J. Wang, Nano Lett. **17**, 6802 (2017).
[54] L. Li, S. Zhang, G. Hu, L. Guo, T. Wei, W. Qin, B. Xiang, C. Zeng, Z. Zhang, and P. Cui, Nano Lett. **22**, 6767 (2022).
[55] P. Baidya, D. Sahani, H. K. Kundu, S. Kaur, P. Tiwari, V. Bagwe, J. Jesudasan, A. Narayan, P. Raychaudhuri, and A. Bid, Phys. Rev. B **104**, 174510 (2021).